

# A Computational Fluid Dynamics–Discrete Element Method Model for Physics-Based Simulation of Structure Formation during Battery Electrode Drying

Silas Wolf,\* Mark Lippke, Alexander Schoo, Arno Kwade, and Carsten Schilde

Drying is a critical process step during battery electrode production due to its microstructure defining nature. Distribution and interconnectivity of active material particles, pores, and the overall porosity significantly influence the later cell performance. Knowledge about structure formation as well as electrode property prediction are crucial for optimization and targeted electrode design. However, the exact microprocesses during electrode drying are not yet understood well and very difficult to access experimentally. Therefore, in this study, a combination of computational fluid dynamics (CFD) and discrete element method (DEM) simulation models for investigating structure formation considering particle–particle as well as fluid–particle interactions and vice versa is presented. The volume of fluid method is used for taking into account the fluid–fluid interface, evaporation and capillary interactions. The simulations reveal the formation of a top–down consolidation front which interacts with the fluid leading to a backflow of liquid. The results show good agreement with experimental measurements for NMC622 cathodes. Furthermore, the influence of production parameters such as mass loading and solids content is examined. The findings demonstrate the modeling tool's suitability for process engineers to anticipate and enhance electrode characteristics and facilitate scientists to understand complex structure formation relationships.

## 1. Introduction


Lithium-ion batteries (LIBs) have become an integral part of our daily lives, not only in the form of powering portable electronics such as laptops and mobile phones, but also in recent years due to the growing demand for electric vehicles.<sup>[1,2]</sup> One of the most important aspects of LIB production is the manufacturing of the electrodes. In particular, their microstructure is an important factor in the subsequent performance of the battery cell, as it must provide space for the lithium ions to diffuse to the active material surface and in parallel sufficient electric pathways. In this regard, a densely packed particle structure favors electrical conduction, which is crucial for the battery cell's charging characteristics, while also leading to higher energy densities.<sup>[3–6]</sup>

Battery electrodes go through a number of steps in the production process before the cells are assembled.<sup>[1,7–10]</sup> The dry components, consisting of active material such as graphite for the anode or lithium–nickel–manganese–cobalt–oxide (NMC) for the cathode, a conductive additive such as carbon black (CB) to create a conductive network, and occasionally the binder responsible for mechanical integrity are usually first dry mixed to form a homogeneous powder mixture.<sup>[11–13]</sup> A solvent, if applicable with already dissolved binder, is then added to form the battery electrode slurry. To homogenize the suspension and disperse particle agglomerates, especially CB, the slurry is subjected to a dispersing step.<sup>[11,14]</sup> After slurry preparation, the suspension is applied to the current collector in a coating step before the porous electrode structure is created by drying the coated suspension film.<sup>[15,16]</sup> At this point, the main structural properties of the particle structure are defined, but the previous process steps already strongly influence the microstructural properties of the electrode.<sup>[6]</sup> To further densify the porous electrode, a calendaring step is often added where the electrode coating is compressed between two rollers to further increase the energy density of the electrode, improve its electronic conductivity and make the coating more uniform.<sup>[17–19]</sup>

The drying process has been the subject of intensive research in the past due to its high energy consumption and its importance for the formation of electrode structure.<sup>[20]</sup> The drying process is typically divided into several stages: After heating up, the

S. Wolf, M. Lippke, A. Schoo, A. Kwade, C. Schilde  
Institute for Particle Technology  
Technische Universität Braunschweig  
Volkmaroder Str. 5, 38104 Braunschweig, Germany  
E-mail: silas.wolf@tu-braunschweig.de

S. Wolf, M. Lippke, A. Schoo, A. Kwade, C. Schilde  
Battery LabFactory Braunschweig  
Technische Universität Braunschweig  
Langer Kamp 19, 38106 Braunschweig, Germany

 The ORCID identification number(s) for the author(s) of this article can be found under <https://doi.org/10.1002/ente.202301004>.

© 2023 The Authors. Energy Technology published by Wiley-VCH GmbH. This is an open access article under the terms of the Creative Commons Attribution-NonCommercial-NoDerivs License, which permits use and distribution in any medium, provided the original work is properly cited, the use is non-commercial and no modifications or adaptations are made.

DOI: 10.1002/ente.202301004

first drying phase, also known as constant rate period, begins. Thereby, the fluid–fluid interface moves with a constant drying velocity due to the constant evaporation rate.<sup>[21]</sup> During this stage, particles become entrapped on the surface as a result of capillary interaction forces present in the three-phase system. In the meantime, particles are subject to sedimentation, even though stabilizing effects due to the present binder and the high slurry viscosity might drastically slow down this process.<sup>[20,22]</sup> According to Stein et al. and Baunach et al., the downward movement of the interface, which usually exceeds the sedimentation rate by orders of magnitude, leads to a top–down consolidation front which ultimately forms the final particulate skeleton of the electrode when it reaches the substrate.<sup>[16,22]</sup> This is typically accompanied by the end of the constant rate period. Although this consolidation theory was also suggested by Jaiser et al., in a later publication they proposed a uniform consolidation mechanism without front formation based on ex situ cryogenic broad ion beam slope cutting in combination with scanning electron microscopy measurements (cryo-BIB–SEM) carried out during graphite anode production.<sup>[15,23]</sup> At the end of the first drying stage, the electrode thickness is fixed (so-called end of solidification) and further reduction of solvent content by pore emptying marks the beginning of the falling rate period. Nevertheless, even though the end of solidification has been reached, a constant drying rate may also prevail during the emptying of the pores due to capillary transport, whereas pore emptying could also already begin while solidification is still ongoing.<sup>[21,24,25]</sup>

One challenge that typically accompanies the structure formation process during drying is migration of the conductive additives and binder: typically, after intensive drying, the inactive components such as binder and conductive additive are unevenly distributed over the thickness of the electrode with depletion near the substrate and accumulation at the coating surface.<sup>[26]</sup> This leads to unfavorable electrode properties such as easy delamination and general low mechanical integrity as well as reduced electrical conductivity.<sup>[22,27,28]</sup> The main processes leading to such segregation behavior are suspected to occur during the constant rate period. This is due to the upward convective movement of solvent caused by solvent evaporation and downward movement of particles.<sup>[26,27,29,30]</sup> In competition, diffusion acts to equalize the resulting concentration gradient.<sup>[22]</sup> Consequently, at high drying rates, the convective movement overtakes the diffusional flux. However, studies by Jaiser et al. and others suggest that capillary transport processes after film solidification are the main mechanisms of additive material segregation.<sup>[31,32]</sup> Based on theoretical findings, a multistage drying process has been developed to reduce binder segregation while ensuring short drying times. This process involves varying drying rates for different segments of the drying process.<sup>[33]</sup>

This evidence suggests that the specific processes of structure formation and additive migration are still a topic of debate in current research, indicating the need for further investigation. Experimental investigations are mostly carried out in a black box process approach, where only the final electrode microstructure is studied and correlated with process or formulation conditions. This is because in situ measurements are difficult and time-consuming. Modeling and simulation could help to better understand the mechanisms and phenomena occurring during battery electrode drying.<sup>[34]</sup> Modeling of the drying process can

cover several aspects: from the simulation of whole dryers over modeling of drying rates to additive segregation models and structure formation investigations. Regarding structure formation in battery electrodes, the first particle-based simulation methods were employed by Zhu et al., who used Brownian dynamics simulations to investigate slurries of manganese oxide active material, CB, and PVDF in NMP to investigate their agglomeration behavior. Cerbelaud et al. followed a similar approach separately for the agglomeration in slurries of silicon nanoparticles and CMC binder or CB.<sup>[35,36]</sup> Structure formation during drying was first modelled by Liu et al. using a 2D coarse-grained lattice-gas model (CGLG) in combination with a kinetic Monte Carlo algorithm.<sup>[37,38]</sup> Active material particles as well as conductive additive particles and binder molecules were considered in a stochastic process of solvent removal and particle rearrangement. The model was able to deliver information about the impact of parameters such as particle morphology, chemical potential (evaporation rate), and binder length on the inner structure. However, these models lack a direct link to physical material and process parameters, making it difficult to use them to support process development. A promising approach was introduced by Forouzan et al. who made use of coarse-grained molecular dynamics (CGMD) to model the interaction between individual active material particles and particles representing the CB-binder domain (CBD) using a combination of the shifted-force Lennard–Jones potential and the granular Hertzian force.<sup>[39]</sup> The solvent was implicitly considered as being part of the CBD particles. The evaporation process was then taken into account by reducing the CBD particle volume and altering their potential parameters. This approach was later further developed by the same group using a smoothed particle hydrodynamics approach to account for the solvent phase and by realizing nonspherical active material shapes.<sup>[40]</sup> The CGMD method was also adapted by the research group of Alejandro A. Franco in a series of studies with the aim of developing a multiscale simulation platform.<sup>[41–46]</sup> These models are able to represent different active material systems, nonspherical particles, and CBD heterogeneities.<sup>[43–46]</sup> However, physical models for fluid–particle and fluid–interface interaction as well as phase change are not taken into account. Srivastava et al. and Lippke et al. used a discrete element method (DEM) approach, where active material and CBD particles were regarded as granular spheres interacting via Hertzian contact forces and cohesive forces.<sup>[47,48]</sup> The fluid in both approaches was considered as an implicit background fluid acting on the particles via Stokesian viscous drag. In case of Srivastava et al., the drying process was simulated by compressing the simulation box from the top until a desired volume fraction was reached. As the simulation approach is therefore unable to predict the final thickness and porosity, the aim of this study was mainly to assess the interaction between the CBD domain and the active material. Lippke et al., on the other hand, used a capillary force model together with a virtual decreasing surface allowing for the prediction of the final coating thickness and microstructural characteristics. However, fluid effects were only considered implicitly and are therefore not thoroughly considered during the structure formation process.

So far, studies on battery electrode drying mainly focused on particle behavior during drying, while mostly omitting the

description of fluid flow. One possibility to describe the behavior of fluids numerically is computational fluid dynamics (CFD). This simulation technique has been widely employed especially to describe the electrochemical and thermal behavior of whole battery cells.<sup>[49–54]</sup> Regarding the manufacturing process of batteries, only a few CFD studies are available, exploring the extrusion process for slurry production,<sup>[55]</sup> electrode coating<sup>[56]</sup> and the electrolyte filling step.<sup>[57–59]</sup> Further CFD studies on the interplay between particles and the surrounding fluid during electrode manufacturing are missing.

The aim of this study is to present a DEM model coupled with CFD to represent granular particle interactions while explicitly considering the effect of fluid flow on structure formation during battery electrode drying. It is therefore possible to capture processes at the fluid–fluid interface and the influence of particle–fluid interactions. This is an advantage over other existing DEM and CGMD models, which either represent the solvent as an implicit background fluid<sup>[47,48]</sup> or as shrinking solvent–CBD particles with no receding liquid surface.<sup>[39,43–46]</sup> Therefore, the proposed model provides a tool for the comprehensive investigation of different materials, formulations, and process parameters to determine their respective influence on the active material structure formation and the drying result. For example, it allows direct investigation of the consolidation process and its effect on the resulting electrode microstructure at the particle scale, which is difficult or impossible to do in the laboratory. The resulting microstructure could also be used as input for subsequent modelling of calendaring, electrolyte filling, and electrochemical behavior, as has been done in similar studies.<sup>[46,59,60]</sup> However, the overall objective of this study is to improve the understanding of structure formation during the drying process.

## 2. Computational Methods

### 2.1. Modeling of Particle Motion

For simulating the behavior of the individual active material particles, the DEM is being used. Developed by Cundall and Strack in 1979, this method enables the description of particle interactions via contact and friction forces. The movement of the individual particles can then be described via the acting forces according to Newton's second law of motion.<sup>[61,62]</sup>

$$m_p \frac{dv_p}{dt} = F_{pp} + F_{pf} + m_p g \quad (1)$$

$$I_p \frac{d\omega_p}{dt} = M_{pp} \quad (2)$$

Here,  $m_p$  and  $v_p$  represent the particle velocity and mass,  $F_{pp}$  and  $F_{pf}$  the particle–particle, respectively fluid–particle force, and  $g$  the gravitational acceleration whereas  $I_p$  and  $\omega_p$  represent the moment of inertia and the angular velocity of the particle, and  $M_{pp}$  the moment acting on the particle due to particle–particle contact. For the particle–particle contact force  $F_{cont}$ , the Hertz–Mindlin contact model in combination with a simplified Johnson–Kendall–Roberts (JKR) cohesion force  $F_{coh}$  was chosen to represent the combined effect of the binder and attractive particle–particle interactions.<sup>[63,64]</sup>

$$F_{pp} = F_{cont} + F_{coh} \quad (3)$$

$$F_{cont} = (k_n \delta_n - \gamma_n v_n) + (k_t \delta_t - \gamma_t v_t) \quad (4)$$

$$F_{coh} = \beta A_c \mathbf{n}_p \quad (5)$$

The elastic constant for normal and tangential contacts is described by  $k_n$  and  $k_t$ , respectively. The overlap distances of two particles in normal and tangential direction are described by  $\delta_n$  and  $\delta_t$ .  $\gamma_n$  and  $\gamma_t$  stand for the viscoelastic damping constants while  $v_n$  and  $v_t$  represent the normal and tangential relative velocities. For the cohesion model, the cohesion energy density  $\beta$  together with the particle contact area  $A_c$  leads to a force in direction of the contact normal vector  $\mathbf{n}_p$ .

The open-source code LIGGGHTS was used to be able to perform the simulations on multiple processors via message passing interface.<sup>[63]</sup> While originally distributed by DCS Computing GmbH, in this work, an academic version published by the Department of Particulate Flow Modeling (PFM, JKU Linz, Austria) was used.

### 2.2. Volume of Fluid Method

Since battery suspensions consist of both particulate material and liquid solvent, coupling CFD with DEM can provide information not only about the interactions between the particles themselves, but also on the interactions between the surrounding fluid and the individual particles. In the special case of the drying process, where a free surface is present, a multiphase CFD method has to be used to account for the fluid–fluid interface. Therefore, the volume of fluid (VOF) method was used, being one of the most widely employed methods to solve multiphase problems such as dam break, gas bubble behavior, or the breaking of waves.<sup>[65]</sup> To do so, each fluid phase is given a volume fraction value  $\alpha$  for each cell. Therefore, an  $\alpha$  value of 1 represents a CFD cell completely filled with the liquid  $i$ , whereas for  $\alpha = 0$ , the cell is filled with the gaseous fluid  $j$ . For values between 0 and 1, an interface between the two fluid phases is present. The VOF method was realized using and further developing the interFoam solver included in OpenFOAM 4, similar to Vångö et al.<sup>[62]</sup>

For the coupling of CFD and DEM, a void fraction value  $\epsilon_f$ , representing the volume fraction of fluid in each CFD cell, is introduced to account for the solids occupancy. This has to be considered in the basic equations of the CFD, where  $u_f$ ,  $\rho_f$ ,  $p_{rg}$  and  $\tau$  stand for, respectively, the fluid velocity, the fluid density, the dynamic pressure, and the liquid–stress tensor. Furthermore, the effect of hydrostatic pressure is considered with  $g$  being the gravitational acceleration and  $\mathbf{x}$  the position vector. The last term on the right-hand side describes the force acting due to the surface tension with the surface tension constant  $\sigma$  and the surface curvature  $\kappa$ .<sup>[62]</sup>

$$\frac{\partial \epsilon_f}{\partial t} + \nabla \cdot (\epsilon_f u_f) = 0 \quad (6)$$

$$\begin{aligned} \frac{\partial \epsilon_f \rho_f u_f}{\partial t} + \nabla \cdot (\epsilon_f \rho_f u_f u_f) \\ = -\epsilon_f \nabla p_{rg} \epsilon_f \nabla \cdot \tau - \epsilon_f g \cdot \mathbf{x} \nabla \rho_f + \sigma \kappa \mathbf{n}_i \end{aligned} \quad (7)$$

The transport equation of the volume fraction  $\alpha_i$  can be described as follows:<sup>[62]</sup>

$$\frac{\partial \alpha_i \varepsilon_f}{\partial t} + \nabla \cdot (\varepsilon_f \alpha_i \mathbf{u}_f) = 0 \quad (8)$$

Based on Equation (8), the position of the interface can then be estimated and the interface curvature can be computed with

$$\kappa = -\nabla \cdot \mathbf{n}_i \quad (9)$$

using the interface normal  $\mathbf{n}_i = \frac{\nabla \alpha_i}{|\nabla \alpha_i|}$ .<sup>[66,67]</sup> The mixed fluid properties are then calculated as follows:<sup>[67]</sup>

$$\rho_f = \alpha_i \rho_i + (1 - \alpha_i) \rho_j \quad (10)$$

$$\eta_f = \alpha_i \eta_i + (1 - \alpha_i) \eta_j \quad (11)$$

To simulate the drying of a suspension, the evaporation of the liquid phase has to be considered on the CFD side. This means that a mass transfer from the liquid to the gas phase needs to be established. Therefore, similar to Breinlinger et al., a source term  $\dot{\alpha}_i$  was introduced on the right-hand side of Equation (8).<sup>[67]</sup>

$$\frac{\partial \alpha_i \varepsilon_f}{\partial t} + \nabla \cdot (\varepsilon_f \alpha_i \mathbf{u}_f) = -\dot{\alpha}_i \varepsilon_f \quad (12)$$

Instead of solving a mass transport equation, for example according to Fick's law, a constantly receding interface with a prescribed drying velocity  $\psi_D$  was assumed, leading to a source term of

$$\dot{\alpha}_i = \frac{\psi_D}{\sqrt{V_C}} \quad (13)$$

with  $V_C$  representing the volume of one CFD cell. To ensure that evaporation only occurs near the interface, the activity of  $\dot{\alpha}_i$  was limited to CFD cells where  $0.01 < \alpha_i < 0.99$ , which ultimately results in a linear decrease of the layer thickness over time.

### 2.3. Coupling Forces

CFD-DEM coupling was realized using the CFDEMcoupling software, originally distributed by DCS Computing GmbH and further developed in an academic version published by the department of particulate flow modeling (PFM, JKU Linz, Austria), as an interconnecting tool between LIGGGHTS and OpenFOAM.<sup>[63]</sup> Coupling between CFD and DEM was achieved in such way, that the drag force exerted by the fluid on the particles or vice versa is taken into account by adding the drag force  $F_d$  of  $n_p$  particles to the momentum Equation (7) in form of a particle-fluid momentum exchange term  $R_{pf} = (\sum_{i=1}^{n_p} F_{d,i}) / V_C$ , leading to the final momentum equation for the CFD-DEM coupling.<sup>[62,63]</sup>

$$\begin{aligned} \frac{\partial \varepsilon_f \rho_f \mathbf{u}_f}{\partial t} + \nabla \cdot (\varepsilon_f \rho_f \mathbf{u}_f \mathbf{u}_f) = & -\varepsilon_f \nabla p_{\text{rgh}} - \varepsilon_f \nabla \cdot \boldsymbol{\tau} \\ & - \varepsilon_f \mathbf{g} \cdot \mathbf{x} \nabla \rho_f + \sigma \kappa \frac{\nabla \alpha_i}{|\nabla \alpha_i|} + R_{pf} \end{aligned} \quad (14)$$

For the drag force, a model by Di Felice was used, which takes into account the drag coefficient  $C_D = (0.63 + 4.8 / \sqrt{Re_p})^2$ ,

the particle diameter  $d_p$ , and the particle Reynolds number

$$Re_p = \frac{\rho_f v_p d_p}{\eta_f} \quad (15)$$

with  $\chi = 3.7 - 0.65 \exp(-0.5(1.5 - \log_{10}(Re_p))^2)$

The drag force as well as additional fluid-particle interaction forces can then be further utilized in the DEM and be added to  $F_{pf}$

$$F_{pf} = F_d + F_c + F_l + F_b \quad (16)$$

In addition to the drag force, a capillary force  $F_c$  is considered in the presented simulation model which represents the effect of the surface tension at the three-phase contact line, when a particle penetrates the fluid-fluid interface. Because of the unresolved nature of the CFD-DEM coupling method, a simplified model by Breinlinger et al. is used. This model does not explicitly account for the curvature of the fluid-fluid interface due to contact angle  $\theta$ , but instead approximates the net force acting in the normal direction of the fluid-fluid interface using the wetting angle  $\omega$  and particle radius  $r_p$ .<sup>[67]</sup> The schematic illustration in **Figure 1** provides more details. According to that, the capillary force can be calculated as follows.

$$F_c = 2\pi r_p \sigma \sin(\omega) \sin(\omega + \theta) \mathbf{n}_i \quad (17)$$

A lubrication force  $F_l$  developed by Kroupa et al. is added to account for the energy dissipated due to the displacement of fluid in the gap in between approaching particles which cannot be resolved via the unresolved CFD-DEM approach.<sup>[69]</sup> The normal part of the lubrication force can be described as follows.

$$F_{l,n} = -6\pi \eta r_p v_r \cdot \mathbf{n}_p \left( \frac{1}{4} 1\delta_r^{-1} - \frac{9}{40} \log(\delta_r) - \frac{3}{112} \delta_r \log(\delta_r) \right) \quad (18)$$

Here,  $v_r$  equals the relative velocity of two approaching particles  $i$  and  $j$ , and  $\delta_r = \frac{d}{r_p}$  the relative distance between the particles using the separation distance  $d = |\mathbf{x}_i - \mathbf{x}_j| - 2r_p$  where  $\mathbf{x}$  is the position vector of the respective particle. More information

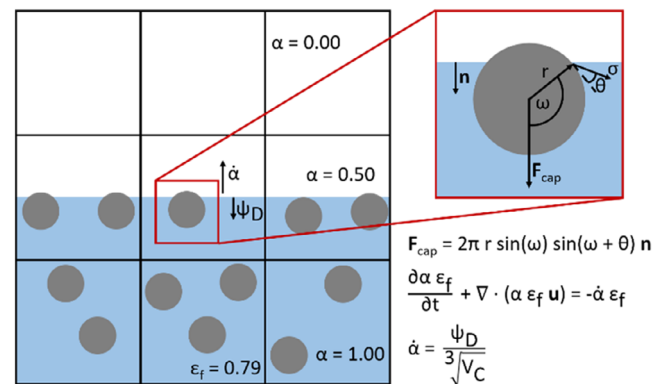


**Figure 1.** Overview over the VOF-DEM coupling method using a capillary force  $F_{cap}$  and a source term in the phase fraction transport equation.

about the force model and its individual components can be found in the respective literature reference.<sup>[69]</sup>

Finally, also a buoyancy force on a particle with volume  $V_p$  has to be taken into account, which is calculated as follows.<sup>[70]</sup>

$$F_b = -g \rho_f V_p \quad (19)$$

#### 2.4. Simulation Setup and Procedure

Since simulating the complete width of an electrode coating is not feasible, a representative volume element (RVE) was developed to keep the computational cost low. Periodic boundary conditions were applied at the sides ( $x$ - and  $y$ -direction) for both the DEM and CFD simulation. The bottom boundary was treated as a wall to account for the current collector foil. The active material particles were represented by a discrete particle size distribution (PSD) of five different size classes. The particle size values were extracted from a continuous PSD from experimental measurements as follows: To reduce the computational cost, the lowest 10% as well as the uppermost 10% of the PSD were cut off. Therefore, all particles below the  $x_{3,10}$  value were considered by a particle size class attributed with a diameter of  $x_{3,10}$  representing 10% of the simulated distribution. The next size class represents the particle sizes between the  $x_{3,10}$  and  $x_{3,30}$  by the mean value of those two and so on. Further information on the PSD discretization can be found in the supporting information.

Apart from the active material particles, during the first drying stage the conductive additive (CB, in this case) is taking part in the structure forming process. Due to its small particle sizes (aggregates of 100–300 nm), considering these as individual discrete elements would lead to immense computational cost. Therefore, coarse-grained CB particles or a similar particulate representation of the CB-binder domain (CBD) are usually used. However, in order to keep the computational cost even lower and because in this study only the active material structure formation is of interest, CB is not treated as individual particles in this case. Instead, the CB phase is assumed to be coated around the active material particles, as observed in several studies.<sup>[6,14]</sup>

Consequently, the viscosity of a pure binder solution was assumed for the surrounding liquid, even though also free CB is expected to be present in the slurry. The implications of this simplified assumption are discussed further below. To represent the porous CB coating around the particles, the radius of the active material particle was enlarged. Typical porosity values of CB after dispersion vary between 30% for high intensive mixing and 80% for low mixing intensities.<sup>[71]</sup> Therefore, a porosity value of 70% was used to calculate the additional CB volume due to the relatively low mixing intensity used in the experiments. From this, the required additional particle radius could be determined iteratively. The exact calculation can be found in the supporting information.

In order to initialize the simulation, particles are placed randomly in the simulation box, until the desired particle number according to solids content and suspension volume is reached. On the CFD side, the mesh was created to satisfy the unresolved CFD–DEM condition. Normally, this would imply a ratio between CFD grid cell length and particle diameter of at least 3. However, at the same time a minimum number of 10 cells per spatial dimension was chosen to ensure a minimum accuracy of CFD simulations. To avoid an excessively large simulation domain and, therefore, save computation time, a cell length/particle diameter ratio of 1.5 was chosen. To ensure numerical stability, a diffusive smoothing approach for the volume fraction and momentum exchange field as described by Vångö et al. was used with a smoothing length of twice the largest particle diameter.<sup>[62]</sup> The  $z$  dimension was chosen to be at least twice the coating thickness and satisfy the aforementioned minimum cell count. To ensure the independence of the simulation result from the CFD mesh parameters, the number of cells and the ratio of CFD cell length-to-particle diameter were varied. Only a minor effect of both parameters on the simulation results was found for the smallest parameter values, as shown in the supporting information. This justifies the presented approach to reduce computational cost. The initial  $\alpha$  values were set to match the theoretical wet film thickness calculated from the solids content and the RVE dimensions. The initialized simulation setup is depicted in **Figure 2** for further clarity.

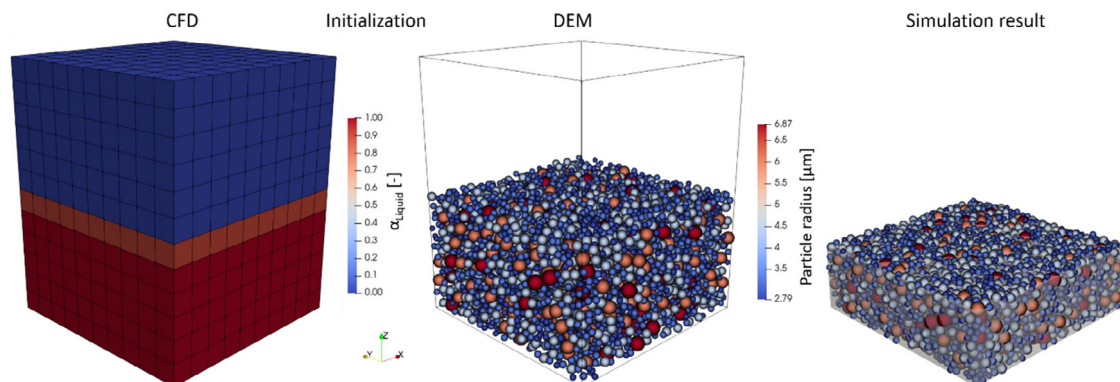


**Figure 2.** Initialized simulation domain for the CFD simulation (left) and DEM simulation (middle). The liquid domain in the CFD grid is indicated by red color whereas the air containing cells are marked with blue color. The position of the interface cells is indicated by the light red color. In the DEM domain, different particle sizes are marked with different colors. On the right, the simulation result after the first drying phase is shown by a combination of the liquid CFD domain (transparent) and the DEM particles.



By applying a constant evaporation rate, the drying process was started. It should be noted, that due to the discrepancy between time and length scale (spatial dimensions in  $\mu\text{m}$  scale, typical drying time 1–2 min), the simulation had to be scaled appropriately to keep the overall simulation time in feasible orders of magnitude. Therefore, the drying rate was scaled up by a factor  $f$  of  $10^5$ . In order to keep the most important force interplays (capillary force, drag force) realistic, the capillary number  $Ca$  was chosen to be constant.

$$Ca = \frac{\eta_f |\nu_p - u_f|}{\sigma} = \text{const.} \quad (20)$$

Since the drying rate, and therefore the particle velocity  $\nu_p$  at the interface is scaled by factor  $f$ , a constant capillary number can be ensured by reducing the dynamic viscosity of the fluid by the same factor, therefore resulting in  $\eta_{f,\text{simulation}} = \eta_{f,\text{real}} / f$ . This comes with several advantages: CB–binder slurries used in battery manufacturing are typically highly viscous liquids with a dynamic viscosity of around 1–30 Pa s.<sup>[72]</sup> In CFD simulations, this would require very small time steps in order to stabilize the simulation resulting in long computation times. Additionally, the sedimentation number

$$N_s = \frac{\nu_{p,\text{sed}}}{\psi_D} = \text{const.} \quad (21)$$

which describes the ratio of the particle sedimentation velocity  $\nu_{p,\text{sed}}$  and the drying velocity  $\psi_D$  is kept constant as well due to the indirect proportionality of  $\nu_{p,\text{sed}}$  and the fluid viscosity according to Stokes' law.<sup>[73]</sup>

## 2.5. Parametrization

In order to assess the ability of the simulation model to predict experimental results, the simulation was set up to represent the drying process of a pilot-scale NMC622 cathode manufacturing process (see Experimental Section). The particle size discretization was performed as described in the earlier section based on laser diffraction measurements. Both the laser diffraction measurement result and the corresponding PSD for the DEM simulation can be taken from the supporting information. Other input values for the particle and solvent properties were chosen to mimic the suspension used for the drying experiments presented in the Experimental Section. Most values were taken from literature or measurement and are listed in Table 1. Instead of the real value for the elastic modulus, a reduced value using a softening factor was chosen to keep the DEM time step low according to the Rayleigh criterion. In the present work, the electrodes were manufactured with the same drying conditions in all of the three drying segments (see Experimental Section). They were chosen similar to the conditions in the second drying section used in the work of Lippke et al.<sup>[48]</sup> Hence, the drying rate calculated for the second dryer segment in Lippke et al. was used for the complete simulation time. As mentioned earlier, due to computational limitations, the drying rate has to be scaled up in the simulations, resulting in a scaling factor to scale down the viscosities. Furthermore, to avoid numerical issues due to large viscosity ratios and low absolute viscosities, the viscosity of the

**Table 1.** Parameter for particle, binder solution, and evaporation properties. The given parameters represent the corresponding values that are expected in experiments. For the simulations, some parameters were scaled with the respective scaling factor according to the scaling methodology explained in the text. If not stated otherwise, values for 20 °C are assumed.

Parameter	Unit	Value
Particle density	$\text{g cm}^{-3}$	4.74 <sup>[79]</sup>
Elastic modulus	GPa	147 <sup>[80]</sup>
Softening factor	–	$10^{-4}$
Friction coefficient	–	0.80 <sup>a)</sup>
Restitution coefficient	–	0.25 <sup>[80]</sup>
Poisson ratio	–	0.25 <sup>[80]</sup>
Cohesion energy density	$\text{N J } \mu\text{m}^{-3}$	400 <sup>a)</sup>
Contact angle	°	24 <sup>[81]</sup>
Liquid dynamic viscosity	Pa s	2 <sup>b)</sup>
Liquid density	$\text{g cm}^{-3}$	1.03 <sup>[82]</sup>
Air dynamic viscosity	Pa s	0.01 liquid viscosity
Air density	$\text{g cm}^{-3}$	$1.20 \times 10^{-3}$
Surface tension	$\text{N m}^{-1}$	40.8
Drying rate	$\mu\text{m}^3 (\mu\text{m}^2 \mu\text{s}^2)^{-1}$	$1.31 \times 10^{-6}$ <sup>[48]</sup>
Scaling factor	–	$10^5$

a) Calibrated; b) Estimation from measurement.

drying air was set two orders of magnitude lower than the viscosity of the binder solution. This is reasonable according to the assumption that the particles are mostly submerged in the solution and air–particle interactions are therefore negligibly small.

As the input values for the cohesion model and the friction are not directly available from experiments, these values had to be calibrated in an iterative process. Therefore, a matrix of different value pairs for the cohesion energy density and the friction coefficient was generated and the corresponding results for the final coating thickness were compared to the experimental values in order to find a suitable value pair. More details on the calibration procedure can be found in the supporting information as well as further details on the numerical simulation parameters.

## 2.6. Postprocessing

For postprocessing the simulations and examining the final electrode properties, the end of the first drying stage had to be identified. This was done by tracking the thickness of the particle layer over time and identifying the time at which the lowest value was reached. Before analyzing the microstructure, the CB coating was deleted by reducing the particle size to the original active material value after the simulation was finished. The particle domain was then divided into 100 segments of equal thickness in  $z$  direction and the particle volume fraction and the porosity for each segment were evaluated. This resulted in a porosity and particle distribution over the coating thickness and allowed for the calculation of a mean and median porosity for the overall

structure. The same method was used to investigate the structure formation progress over time. For this, the spatial microstructure distribution was evaluated for four different equidistant points in time.

### 3. Results and Discussion

#### 3.1. Structure Formation Process

To begin the investigation of the structure formation process, first the evolution of the coating thickness is examined. **Figure 3a** shows the temporal evolution of the particles at the highest position in the DEM simulation. As expected, the curve follows a linear decrease over time. This is due to the constant evaporation rate during the first drying stage, which drives the liquid surface with a constant speed into the direction of the current collector. Since a capillary force is acting when particles approach the fluid–fluid interface, the particles get trapped underneath the surface. Therefore, some minor oscillations are visible due to particle rearrangement under the influence of capillary, interparticle, and fluid–particle forces in the resulting particle packing. Once the first drying period is over, the particle packing cannot be further compressed by the capillary forces due to the resisting interparticulate forces and the coating thickness stays nearly constant. This typically marks the transition to the second drying stage. To provide more insight, the rendered CFD-DEM simulation images in **Figure 3a** further visualize the drying progress and the transition to the second drying phase on the particle scale. When reaching the end of the first drying stage,  $t_{\text{End}}$ , the interface starts to recede below the uppermost particle layer. The resulting particle skeleton is therefore no longer exposed to capillary forces and expands slightly as a consequence. However, the unresolved CFD-DEM method cannot directly depict the contact angle on the CFD side. Additionally, it is unable to adapt to changes in drying kinetics during pore emptying. Consequently, the behavior after the end of the first drying stage can no longer physically represent reality. Therefore, all further investigations are done by taking  $t_{\text{End}}$  as the point of interest.

To investigate the evolution of the microstructure during the first drying stage more deeply, the profile of particle volume fraction over the film thickness is depicted in **Figure 3b**. For this purpose, the four equidistant points in time marked in **Figure 3a** were chosen. As already mentioned, particles interact with the two-phase boundary and get pulled downward by the capillary force. This leads to an increase in particle volume fraction up to a maximum value often referred to as “jamming point”, which refers to the transition of the particle suspension from a fluid-like state to a rigid, contact dominated state.<sup>[74]</sup> The result is the formation of what is known as a consolidation layer, consisting of densely packed particles that cannot rearrange much further. While this is difficult to observe in the simulation images, **Figure 3b** shows the increase in particle volume fraction in the vicinity of the interface during the drying progress. As it collects more and more particles during drying, this consolidation front grows in thickness until it ultimately reaches the substrate. At this point, it gets further compressed and forms the fully consolidated particle structure at the end of the constant drying rate period. By looking at the final particle structure, an increase in electrode density toward the top of the coating is observed. This could be an effect of the consolidation front formation during drying, where the particles captured early on in the process have more time available for rearranging into a densely packed structure near the interface.

A similar structure formation mechanism was proposed by Jaiser et al., called “top–down consolidation”.<sup>[23]</sup> However, it was rejected in a subsequent study due to cryo-BIB-SEM measurements, indicating a uniform consolidation over the whole coating thickness.<sup>[15]</sup> They explained this by the fact, that the high slurry viscosity and possible polymer binder networks due to the binder could stabilize the slurry against sedimentation and also prevent the formation of a consolidation front. Nevertheless, they also observed an increase in particle volume fraction toward the coating surface in the final dried electrode structure. It should be noted that the investigated system in the described work differs from the study presented here, since graphite anodes were examined instead of NMC cathodes. Additionally, as already mentioned, the choice of rheological liquid properties for the

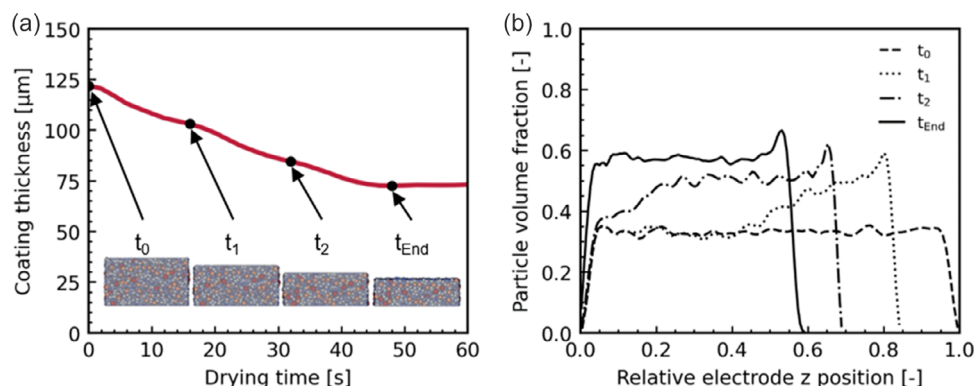


**Figure 3.** a) Evolution of coating thickness over drying time. The four equidistant time points for analyzing the structure formation progress are marked. Simulation images show the state of particle consolidation with the liquid phase displayed as a transparent box. b) Particle volume fraction in the analyzed segments over relative electrode thickness with respect to the starting wet film thickness. Results are shown for the four evaluation points marked in (a) to map the structure formation process.

simulations is challenging and could further impact the structure formation process. Therefore, the matter of the fluid impact on the structure formation process is further discussed in the following section.

### 3.2. Fluid Impact on Structure Formation

Since in the presented model a two-way coupling approach is used, which incorporates fluid–particle as well as particle–fluid interaction, a comparison with a one-way approach can elucidate the effect of fluid motion on the structure formation process. When using one-way coupling, the void fraction  $\varepsilon_f$  is set to 1 and the momentum exchange term  $R_{pf}$  is neglected. Therefore, the fluid only influences the particle movement, but is not influenced by the particles in any way. In **Figure 4**, the structure formation process of the two different approaches is compared. In this case, the same analysis time points are chosen except for  $t_{\text{End}}$ , based on an equidistant division from start to end of the constant rate period of the two-way case. Starting from the same particle distribution in both cases, minor differences become apparent already at time  $t_1$ . An overall higher particle

fraction toward the fluid–fluid interface is observable here in case the particle–fluid interactions are taken into account. This leads to a faster growing consolidation front in the one-way case which reaches the bottom already at time  $t_2$ , in contrast to the two-way case. Ultimately, this leads to a slightly thicker electrode with a more porous structure for the one-way case. To make sure that the differences in the consolidation process are not of stochastic nature, two-way coupled simulations initialized with different random positions were compared. The results, which can be found in the supporting information, delivered no significant deviation for the different initializations. It was therefore concluded that the fluid flow had a significant influence on structure formation.

In order to further clarify the fluid influence on structure formation, in **Figure 4b** the mean value for the  $z$  component of the fluid velocity inside the liquid domain of the CFD simulation is plotted over time. Due to the lack of acting forces and fluid replacement, the liquid velocity shows only small oscillations around 0 in case the one-way coupling approach is used. For the two-way coupling case instead, a rise in liquid velocity in positive  $z$  direction (toward the film surface) can be observed until the end of the first drying stage. Since the velocity mostly reaches positive values up to  $1.3 \mu\text{m s}^{-1}$  (close to the drying rate), an upward fluid flow appears to develop that opposes the downward movement of the particles. Therefore, particle movement in the negative  $z$ , and thus, downward direction is hindered due to the acting drag forces. Similar conclusions were also drawn in previous studies investigating stratification phenomena of colloidal suspensions.<sup>[75,76]</sup> This could lead to further compression of the consolidation layer from below, resulting in a thinner, denser consolidation front and, ultimately, a less porous particle structure.

As already mentioned before, also the viscosity of the interstitial fluid is strongly related to formulation parameters such as initial binder content, CB content, dispersion state and overall solids content. Furthermore, due to evaporation the rheological properties of the electrode slurry change during the drying process. Depicting the correct rheological behavior in simulation is therefore challenging, which is the reason why in the presented simulations the dynamic viscosity was kept at a constant value of 2 Pa s for all variations. However, in order to gain an understanding of the influence of liquid viscosity on the structure formation process, two example simulations with liquid viscosities of 0.5 and 5 Pa s were carried out and compared. These could, for example, represent slurries with varying binder or CB content.<sup>[72]</sup>

The results for the consolidation process with different liquid viscosities are depicted in **Figure 5**. When comparing the structure formation process, the most vivid difference lies in the distribution of particles during the build up of the consolidation layer. For the higher viscosity case, a spike in solids volume fraction toward the fluid surface becomes visible early on. When using a lower liquid viscosity, a smoother solid distribution inside the consolidation front can be observed. Also, similar to the comparison between one-way and two-way coupled simulations discussed before, the consolidation front in the lower viscous case reaches the substrate earlier, whereas the solids fraction difference in the whole range of the consolidated region is not as pronounced as in the highly viscous case. This suggests an opposed effect to the explanations by Jaiser et al. discussed in

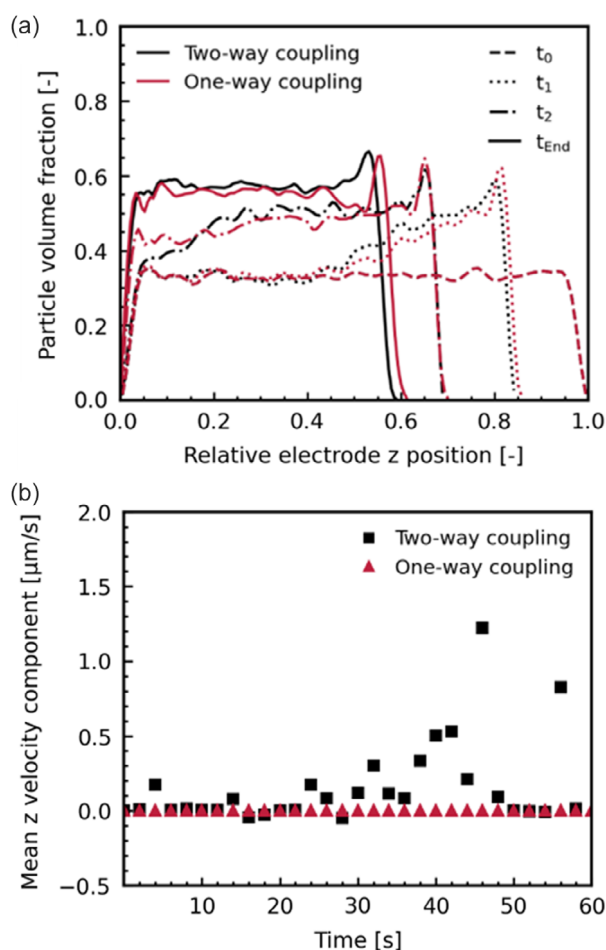


**Figure 4.** a) Consolidation progress using the one-way coupling and the two-way coupling method. Except for the end time, the same points of time were used for analysis. b) Mean value of the  $z$  component of liquid velocity using two-way and one-way coupling.



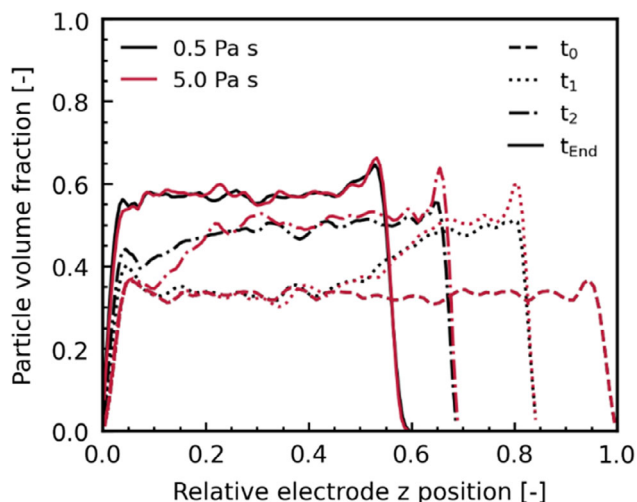


**Figure 5.** Consolidation behavior of suspensions with different liquid viscosities.

the previous section, where higher liquid viscosities were related to a homogeneous solidification in their anode-based system.

When using higher liquid viscosities, the particles in the slurry experience higher drag forces during drying. This means that the propagation of the consolidation front toward the substrate is hindered, both by drag forces due to interfacial movement and by fluid backflow. As a result, the particles tend to accumulate directly at the fluid–fluid interface, forming a densely packed layer. Additionally, lower viscosities lead to a stronger influence of particle sedimentation, which could enhance the differences in consolidation behavior. However, during the final compression of the consolidated particle layer at the end of the first drying phase, the differences seem to disappear. Therefore, no impact of liquid viscosity on the final microstructure could be observed, at least in the case of the examined suspensions.

### 3.3. Comparison to Manufacturing Results for Different Mass Loadings

In order to verify the validity of the CFD–DEM model, the simulation results were compared with experimental results for different mass loadings produced as described in the experimental section. **Figure 6a** shows a parity plot displaying simulation results for the final electrode thickness over the coating thicknesses measured from the electrodes produced in experiments. Most of the points are in close vicinity to the parity line, indicating a very good agreement between experimental and simulated results. However, only the result coming from the calibration simulations (red marker) shows a perfect resemblance as expected since this value was used to find the optimum value pairs for friction and cohesion contact model parameters. The validation results indicate a very slight underestimation of the coating thickness, nevertheless with deviations mostly in the range of one standard deviation of the results. Additionally, the porosity in between the active material  $\varepsilon_{AM}$  was estimated from the thicknesses in the experiments using the mass loading of the

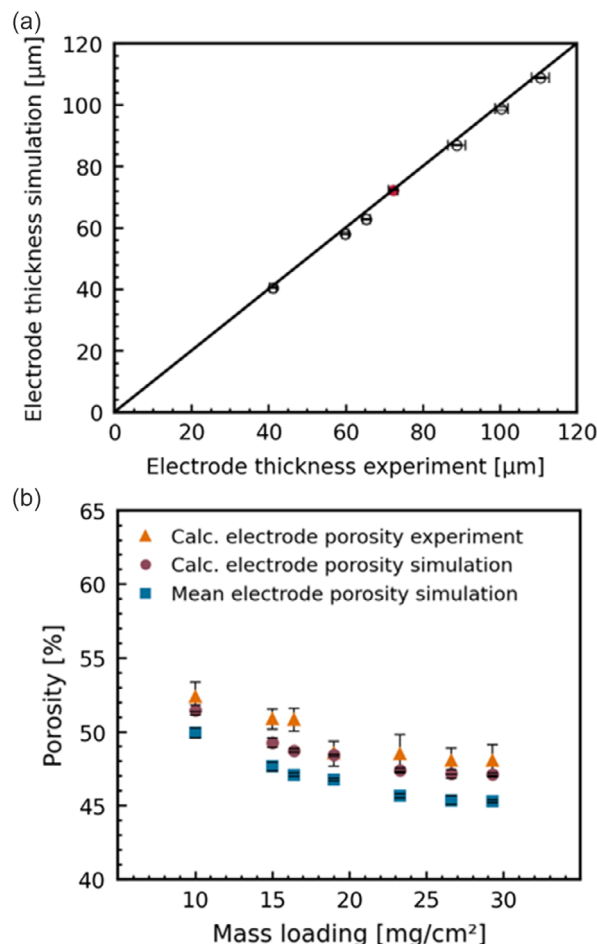


**Figure 6.** a) Parity plot of simulated electrode thickness and reference results from experiments for different mass loadings. The red marker illustrates the value used for calibration. The diagonal parity line indicates perfect correlation. b) Comparison of porosities in between the active material particles estimated based on calculations from coating thicknesses in the experiments, simulation, and from the mean value of the porosity distribution in  $z$  direction dependent on the mass loading.

active material  $ML_{AM}$ , the coating thickness  $t_c$ , and the active material density  $\rho_{AM}$

$$\varepsilon_{AM} = 1 - \frac{ML_{AM}}{\rho_{AM} t_c} \quad (22)$$

The aforementioned process was then replicated for the coatings produced via CFD–DEM simulations, based on the coating thickness attained. In **Figure 6b**, a comparison between the calculated active material porosity in the experiment and in the simulation is presented. Moreover, the mean porosity value resulting from the segment-wise porosity estimation described earlier is shown for comparison. Since the calculated porosity according to Equation (22) is directly dependent on the coating thickness, the simulations and experiments are in good agreement. Apart from a slight underestimation of the porosity due to the aforementioned underestimation of the coating thickness, the

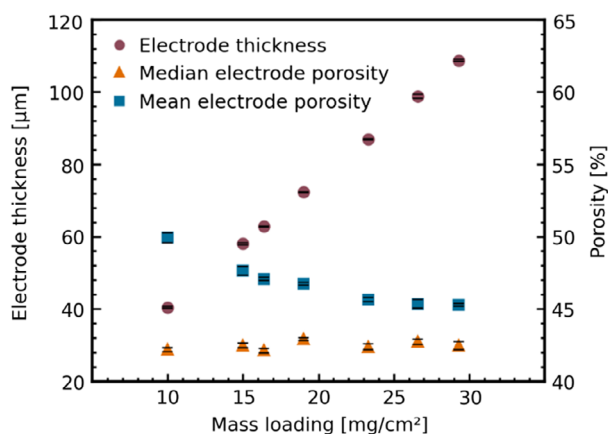


**Figure 7.** Electrode thickness and porosity values resulting from simulations of the different target mass loadings used for validation.

course of decreasing porosities with higher mass loadings is captured accurately not only by the porosity calculated with Equation (22), but also when using the segment-wise analysis. The larger absolute error here is most likely due to uncertainties when assuming the CB porosities used in the simulations, which directly impacts the segment-wise porosity calculations.

The simulations describe very well the trend of linearly increasing layer thicknesses expected with increasing target mass loadings. This is also shown in **Figure 7**, together with results for the median and mean porosity values of the resulting coating. Since a linear increase of coating thickness with constant material densities should lead to more or less constant coating densities, the porosity of the electrode remains constant at least when taking a look at the median values. The mean porosity values, however, show an asymptotic decrease for increasing mass loadings as already mentioned before. This is due to boundary effects (lack of particles intruding the segments near current collector and surface from below and above). **Figure 8** shows the porosity distribution over the final electrode thickness for the reference

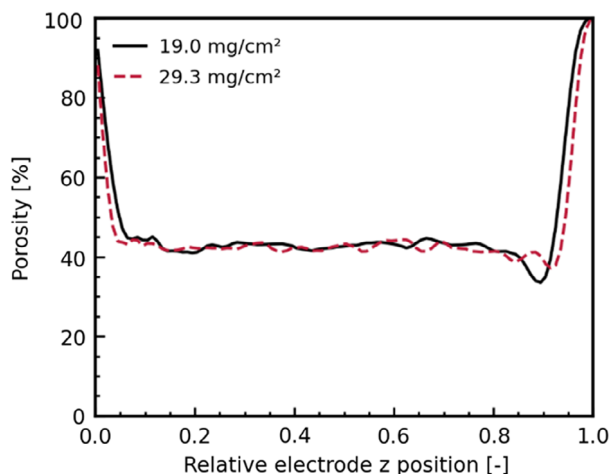


**Figure 8.** Porosity of segments over the relative electrode  $z$  position related to the final coating thickness. Results for two different target mass loadings are shown.

case with a mass loading of  $19.0 \text{ mg cm}^{-2}$  and a thicker electrode ( $29.3 \text{ mg cm}^{-2}$ ). For the thinner electrode, the aforementioned porous boundary regions are shifted toward the inner region compared to the thicker electrode. Therefore, the porous segments have a greater effect on the average porosity calculation, resulting in a higher overall porosity. Thus, the median porosity value is more suitable to describe the inner electrode porosity. However, comparing the mean and the median value could be helpful to describe porosity gradients on a global scale.

### 3.4. Influence of Solids Content

Apart from the targeted mass loading, the solid content was varied in simulations while keeping a constant target mass loading of  $19.0 \text{ mg cm}^{-2}$ . The results for the electrode thickness and the porosity values for this kind of parameter study can be taken from **Figure 9**. For solids contents up to 65 wt%, no significant influence on the macroscopic electrode properties is observable. For higher solids contents though, a decrease in coating thickness and porosity can be recognized. This is consistent with the work of Haarmann et al., who varied the solids content in an electrode manufacturing process using an extruder to disperse the electrode slurry.<sup>[77]</sup> While they observed a drop in porosity at higher solids contents, they attributed this to increased deagglomeration of the CB agglomerates due to increasing slurry viscosity. However, in the present simulation study, the dispersing state of the CB agglomerates is not changed for different solids contents. The drop in electrode thickness and porosity must therefore stem from a different phenomenon.

**Figure 10** shows the layer development process similar to **Figure 4b**. However, some differences can be observed: In the reference case with a solids content of 70 wt%, a clear consolidation front develops and further increases from top to down with particles jamming at a solid fraction of around 0.50. In the now considered case, due to the high solids content, the initial particle volume fraction already reaches values of around 0.45, which is close to the jamming point of the reference case. During consolidation, therefore, an already weak particle contact network is established early on, leading to a less pronounced consolidation

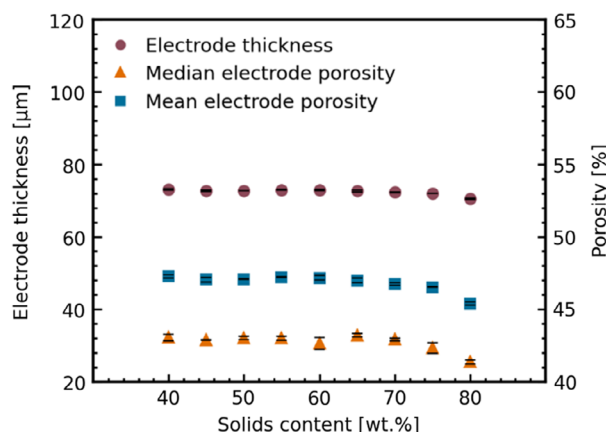


**Figure 9.** Coating thickness and porosity values resulting from simulations of different slurry solids contents using the same target mass loading of  $19.0 \text{ mg cm}^{-2}$ .

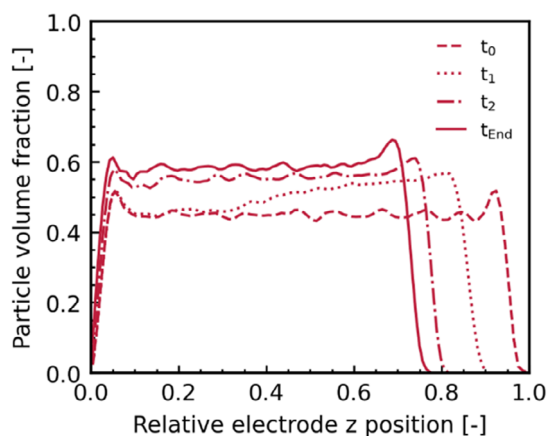


**Figure 10.** Consolidation process for a slurry solids content of 80 wt%.

front with a jamming volume fraction of about 0.55. This layer then rapidly reaches the substrate and is further compressed by the interface movement, resulting in a more compact particle coating. The described process is therefore much more similar to the theory explained by Jaiser et al., where a clear top-down consolidation process was not visible, as explained earlier.<sup>[15]</sup> However, it should be noted that a change in the solids content of the slurry should also result in a change in the viscosity of the interstitial fluid, which could also lead to differences in consolidation behavior, as discussed earlier, and has not been taken into account here. Also, polymer networks that are not taken into account in the current simulation setup could alter the consolidation behavior especially in such densely packed slurries, so that an even more homogeneous consolidation could be observed as suggested by Jaiser et al.

## 4. Conclusion

In this work, a CFD-DEM model to investigate the structure formation during the drying step in the Li-Ion battery electrode manufacturing chain was presented. To realize interactions between particles and the fluid–fluid interface, the VOF method was used and coupled to DEM. A capillary force model was used to capture the mechanisms at a three-phase contact line. To take into account liquid evaporation, a negative source term was added to the VOF transport equation. These extensions to the VOF method enabled the study of the layer formation process.

The simulation output allows the investigation of various structural properties such as porosity versus thickness, its mean and median values, and coating thickness. Results were obtained not only for the final coating, but also during the stratification process. Application to a reference cathode manufacturing process verified the applicability of the simulation model to real-world scenarios. The model was able to predict the coating thickness of electrodes with varying target mass loadings. Furthermore, investigations of the structure formation process revealed the build-up of a top-down consolidation layer resulting in a density gradient within the electrode structure. Since the simulation models used a two-way-coupled CFD-DEM approach, the effect of fluid backflow resulting from the downward

movement of the consolidation layer could be captured in contrast to a comparable one-way simulation setup. When using a two-way coupling approach, a slightly denser consolidation front was observed, leading to a thinner, denser coating. Similar effects could be observed for cases, in which the liquid viscosity was varied. Higher viscosities lead here to an increase of solid content near the interface during structure formation. However, these effects did not reflect in the final microstructure.

In order to prove the applicability of the model to estimate the influence of production parameters on electrode properties, the target mass loading and solids content were varied. The mass loading variations lead to a linear increase of coating thickness with rising mass loadings as expected for such manufacturing variations. Higher mean porosities for thinner electrodes can be explained by a larger influence of porous regions near the substrate and the electrode surface. Variations of the solids content using a constant target mass loading revealed a decrease in coating thickness and porosity for high solids contents. This was accompanied by a less pronounced consolidation front due to the initially high particle volume fraction. Therefore, the film consolidated in a more uniform manner, leading to a denser coating.

In summary, it has been successfully demonstrated that the presented CFD-DEM coupling method is a useful tool to elucidate the structure formation process and predict and optimize the electrode structures for different production parameters. To further investigate the structure formation mechanisms and especially the fluid influence in more detail, resolved CFD-DEM coupling simulations could be helpful in the future. This could also help to further reveal the impact of the rheological properties on the consolidation process. Furthermore, the advantages of using a CFD approach to depict the fluid phase could be explored even further, for example, by including equations for binder migration and explicitly taking into account phase change dependence on drying conditions.

## 5. Experimental Section

**Cathode Materials:** The formulation was based on three different materials, with the active material (NCM622) forming the highest proportion at 96 wt%. To increase the electrical conductivity, 1 wt% CB (C65) was added and 3 wt% binder to improve the mechanical integrity (PVDF 5130).

**Cathode Slurry Preparation:** To prepare the electrode slurry, all components were dry homogenized for 15 min at 49 min<sup>−1</sup> in a 3D shaking mixer (Willy A. Bachofen AG, Turbula T2F). The dispersion process was carried out in a dissolver (VMA-Getzmann, DISPERMAT CA60) at a solid content of 70 wt%. The powder mixture was successively added to the solvent (NMP) and then dispersed at a tangential velocity of 9 m s<sup>−1</sup> for 45 min. In a final step, the suspension was degassed at a tangential velocity of 3 m s<sup>−1</sup> for 15 min.

**Coating and Drying Setup:** The coating of the prepared electrode suspension was carried out on a 15 µm-thick aluminum substrate through a combbar reverse roll coating process. It was then dried in a 6 m convective dryer (KROENERT GmbH & Co. KG, LabCo) with constant drying conditions for all of the three dryer sections at a web speed of 1 m min<sup>−1</sup> and 100 °C. The airflow was in impingement-free mode with a fan power of 60 %. The different basis weights were achieved by a successive increase in the doctor blade gap, and the film thickness was determined with a digital dial gauge.

For more details about the electrode production process, the reader is referred to Haselrieder et al.<sup>[78]</sup>

## Supporting Information

Supporting Information is available from the Wiley Online Library or from the author.

## Acknowledgements

The authors gratefully acknowledge financial support from the European Union's Horizon 2020 Research and Innovation Pro-gramme within the project "DEFACTO" (grant no. 875247). The authors would also like to thank the Deutsche Forschungsgemeinschaft (DFG) in the context of the Heisenberg Program SCHI 1265/19-1 "Digital methods for complex systems in process and production engineering". Furthermore, this work used the Phoenix high performance cluster and was supported by the Gauß-IT-Zentrum of the Technical University of Braunschweig (GITZ). Moreover, the valuable assistance of Dimitri Ivanov in modeling the lubrication forces is acknowledged.

Open Access funding was enabled and organized by Projekt DEAL.

## Conflict of Interest

The authors declare no conflict of interest.

## Data Availability Statement

The data that support the findings of this study are available from the corresponding author upon reasonable request.

## Keywords

CFD-DEM coupling, drying, lithium-ion battery, structure formation, volume of fluid method

Received: August 22, 2023

Revised: November 28, 2023

Published online:

- [1] A. Kwade, W. Haselrieder, R. Leithoff, A. Modlinger, F. Dietrich, K. Droeder, *Nat. Energy* **2018**, *3*, 290.
- [2] C. P. Grey, D. S. Hall, *Nat. Commun.* **2020**, *11*, 6279.
- [3] B. G. Westphal, N. Mainusch, C. Meyer, W. Haselrieder, M. Indrikova, P. Titscher, H. Bockholt, W. Viöl, A. Kwade, *J. Energy Storage* **2017**, *11*, 76.
- [4] G. Inoue, M. Kawase, *J. Power Sources* **2017**, *342*, 476.
- [5] H. Kondo, H. Sawada, C. Okuda, T. Sasaki, *J. Electrochem. Soc.* **2019**, *166*, A1285.
- [6] H. Bockholt, M. Indrikova, A. Netz, F. Golks, A. Kwade, *J. Power Sources* **2016**, *325*, 140.
- [7] J. Li, J. Fleetwood, W. B. Hawley, W. Kays, *Chem. Rev.* **2022**, *122*, 903.
- [8] R. Gonçalves, S. Lanceros-Méndez, C. M. Costa, *Electrochem. Commun.* **2022**, *135*, 107210.
- [9] S. N. Bryntesen, A. H. Strømman, I. Tolstorebrov, P. R. Shearing, J. J. Lamb, O. Stokke Burheim, *Energies* **2021**, *14*, 1406.
- [10] W. B. Hawley, J. Li, *J. Energy Storage* **2019**, *25*, 100862.
- [11] H. Bockholt, W. Haselrieder, A. Kwade, *ECS Trans.* **2013**, *50*, 25.
- [12] W. Bauer, D. Nötzel, V. Wenzel, H. Nirschl, *J. Power Sources* **2015**, *288*, 359.
- [13] M. Wang, D. Dang, A. Meyer, R. Arsenault, Y.-T. Cheng, *J. Electrochem. Soc.* **2020**, *167*, 100518.
- [14] J. K. Mayer, L. Almar, E. Asylbekov, W. Haselrieder, A. Kwade, A. Weber, H. Nirschl, *Energy Technol.* **2019**, *8*, 1900161.
- [15] S. Jaiser, J. Kumberg, J. Klaver, J. L. Urai, W. Schabel, J. Schmatz, P. Scharfer, *J. Power Sources* **2017**, *345*, 97.
- [16] M. Stein IV, A. Mistry, P. P. Mukherjee, *J. Electrochem. Soc.* **2017**, *164*, A1616.
- [17] T. Marks, S. Trussler, A. J. Smith, D. Xiong, J. R. Dahn, *J. Electrochem. Soc.* **2011**, *158*, A51.
- [18] W. Haselrieder, S. Ivanov, D. K. Christen, H. Bockholt, A. Kwade, *ECS Trans.* **2013**, *50*, 59.
- [19] C. Meyer, H. Bockholt, W. Haselrieder, A. Kwade, *J. Mater. Process. Technol.* **2017**, *249*, 172.
- [20] Y. S. Zhang, N. E. Courtier, Z. Zhang, K. Liu, J. J. Bailey, A. M. Boyce, G. Richardson, P. R. Shearing, E. Kendrick, D. J. L. Brett, *Adv. Energy Mater.* **2022**, *12*, 2102233.
- [21] C. Zihurul, S. Wolf, A. Kwade, *Energy Technol.* **2023**, *11*, 2200671.
- [22] M. Baunach, S. Jaiser, S. Schmelzle, H. Nirschl, P. Scharfer, W. Schabel, *Drying Technol.* **2016**, *34*, 462.
- [23] S. Jaiser, M. Müller, M. Baunach, W. Bauer, P. Scharfer, W. Schabel, *J. Power Sources* **2016**, *318*, 210.
- [24] S. Jaiser, L. Funk, M. Baunach, P. Scharfer, W. Schabel, *J. Colloid Interface Sci.* **2017**, *494*, 22.
- [25] L. Pfaffmann, S. Jaiser, M. Müller, P. Scharfer, W. Schabel, W. Bauer, F. Scheiba, H. Ehrenberg, *J. Power Sources* **2017**, *363*, 460.
- [26] B. G. Westphal, A. Kwade, *J. Energy Storage* **2018**, *18*, 509.
- [27] C.-C. Li, Y.-W. Wang, *J. Electrochem. Soc.* **2011**, *158*, A1361.
- [28] J. Landesfeind, A. Eldiven, H. A. Gasteiger, *J. Electrochem. Soc.* **2018**, *165*, A1122.
- [29] F. Font, B. Protas, G. Richardson, J. M. Foster, *J. Power Sources* **2018**, *393*, 177.
- [30] Z. Zhu, Y. He, H. Hu, *J. Phys. D: Appl. Phys.* **2021**, *54*, 55503.
- [31] J. Klemens, L. Schneider, E. C. Herbst, N. Bohn, M. Müller, W. Bauer, P. Scharfer, W. Schabel, *Energy Technol.* **2022**, *10*, 2100985.
- [32] H. Hagiwara, W. J. Suszynski, L. F. Francis, *J. Coat. Technol. Res.* **2014**, *11*, 11.
- [33] S. Jaiser, A. Friske, M. Baunach, P. Scharfer, W. Schabel, *Drying Technol.* **2017**, *35*, 1266.
- [34] P. S. Grant, D. Greenwood, K. Pardikar, R. Smith, T. Entwistle, L. A. Middlemiss, G. Murray, S. A. Cussen, M. J. Lain, M. J. Capener, M. Copley, C. D. Reynolds, S. D. Hare, M. J. H. Simmons, E. Kendrick, S. P. Zankowski, S. Wheeler, P. Zhu, P. R. Slater, Y. S. Zhang, A. R. T. Morrison, W. Dawson, J. Li, P. R. Shearing, D. J. L. Brett, G. Matthews, R. Ge, R. Drummond, E. C. Tredenick, C. Cheng, et al., *J. Phys. Energy* **2022**, *4*, 42006.
- [35] M. Cerbelaud, B. Lestriez, D. Guyomard, A. Videcoq, R. Ferrando, *Langmuir* **2012**, *28*, 10713.
- [36] M. Cerbelaud, B. Lestriez, A. Videcoq, R. Ferrando, D. Guyomard, *J. Electrochem. Soc.* **2015**, *162*, A1485.
- [37] Z. Liu, P. P. Mukherjee, *J. Electrochem. Soc.* **2014**, *161*, E3248.
- [38] Z. Liu, D. L. Wood, P. P. Mukherjee, *Phys. Chem. Chem. Phys.* **2017**, *19*, 10051.
- [39] M. M. Forouzan, C.-W. Chao, D. Bustamante, B. A. Mazzeo, D. R. Wheeler, *J. Power Sources* **2016**, *312*, 172.
- [40] M. Nikpour, N. Barrett, Z. Hillman, A. I. Thompson, B. A. Mazzeo, D. R. Wheeler, *J. Electrochem. Soc.* **2021**, *168*, 60547.
- [41] A. C. Ngandjong, A. Rucci, M. Maiza, G. Shukla, J. Vazquez-Arenas, A. A. Franco, *J. Phys. Chem. Lett.* **2017**, *8*, 5966.
- [42] A. Rucci, A. C. Ngandjong, E. N. Primo, M. Maiza, A. A. Franco, *Electrochim. Acta* **2019**, *312*, 168.
- [43] T. Lombardo, A. C. Ngandjong, A. Belhcn, A. A. Franco, *Energy Storage Mater.* **2021**, *43*, 337.

- [44] T. Lombardo, F. Lambert, R. Russo, F. M. Zanotto, C. Frayret, G. Toussaint, P. Stevens, M. Becuwe, A. A. Franco, *Batteries Supercaps* **2022**, 5, e202200116.
- [45] J. Xu, A. C. Ngandjong, C. Liu, F. M. Zanotto, O. Arcelus, A. Demortière, A. A. Franco, *J. Power Sources* **2023**, 554, 232294.
- [46] C. Liu, O. Arcelus, T. Lombardo, H. Oularbi, A. A. Franco, *J. Power Sources* **2021**, 512, 230486.
- [47] I. Srivastava, D. S. Bolintineanu, J. B. Lechman, S. A. Roberts, *ACS Appl. Mater. Interfaces* **2020**, 12, 34919.
- [48] M. Lippke, T. Ohnimus, T. Heckmann, D. Ivanov, P. Scharfer, W. Schabel, C. Schilde, A. Kwade, *Energy Technol.* **2022**, 11, 2200724.
- [49] Y. Jiang, L. Zhang, G. Offer, H. Wang, *Digital Chemical Engineering* **2022**, 5, 100055.
- [50] G. Li, S. Li, *ECS Trans.* **2015**, 64, 1.
- [51] E. Gümüşsu, Ö. Ekici, M. Köksal, *Appl. Therm. Eng.* **2017**, 120, 484.
- [52] L. Magri, L. Sequino, C. Ferrari, *Batteries* **2023**, 9, 397.
- [53] A. R. Sharma, C. S. Sai, A. Kumar, R. V. Jayasimha Reddy, D. Danyharsha, R. Jilte, *Mater. Today: Proc.* **2021**, 46, 10964.
- [54] E. Solai, H. Beaugendre, U. Bieder, P. M. Congedo, *Appl. Therm. Eng.* **2023**, 220, 119656.
- [55] J. F. Meza Gonzalez, H. Nirschl, *Energy Tech.* **2023**, 11, 2201517.
- [56] A. Hoffmann, S. Spiegel, T. Heckmann, P. Scharfer, W. Schabel, *J. Coat. Technol. Res.* **2023**, 20, 3.
- [57] M. P. Lautenschlaeger, B. Prifling, B. Kellers, J. Weinmiller, T. Danner, V. Schmidt, A. Latz, *Batteries Supercaps* **2022**, 5, e202200090.
- [58] J. Hagemeister, F. J. Günter, T. Rinner, F. Zhu, A. Papst, R. Daub, *Batteries* **2022**, 8, 159.
- [59] A. Shodiev, E. Primo, O. Arcelus, M. Chouchane, M. Osenberg, A. Hilger, I. Manke, J. Li, A. A. Franco, *Energy Storage Mater.* **2021**, 38, 80.
- [60] M. Chouchane, A. Rucci, T. Lombardo, A. C. Ngandjong, A. A. Franco, *J. Power Sources* **2019**, 444, 227285.
- [61] P. A. Cundall, O. D. L. Strack, *Geotechnique* **1979**, 29, 47.
- [62] M. Vångö, S. Pirker, T. Lichtenegger, *Appl. Math. Model.* **2018**, 56, 501.
- [63] C. Kloss, C. Goniva, A. Hager, S. Amberger, S. Pirker, *Prog. Comput. Fluid Dyn.* **2012**, 12, 140.
- [64] T. Roessler, A. Katterfeld, *Particuology* **2019**, 45, 105.
- [65] C. W. Hirt, B. D. Nichols, *J. Comput. Phys.* **1981**, 39, 201.
- [66] S. S. Deshpande, L. Anumolu, M. F. Trujillo, *Comput. Sci. Disc.* **2012**, 5, 14016.
- [67] T. Breinlinger, A. Hashibon, T. Kraft, *Powder Technol.* **2015**, 283, 1.
- [68] Z. Y. Zhou, S. B. Kuang, K. W. Chu, A. B. Yu, *J. Fluid Mech.* **2010**, 661, 482.
- [69] M. Kroupa, M. Vonka, M. Soos, J. Kosek, *Langmuir* **2016**, 32, 8451.
- [70] J. Zhao, T. Shan, *Powder Technol.* **2013**, 239, 248.
- [71] J. K. Mayer, H. Bockholt, A. Kwade, *J. Power Sources* **2022**, 529, 231259.
- [72] Q. Liu, J. J. Richards, *J. Rheol.* **2023**, 67, 647.
- [73] C. M. Cardinal, Y. D. Jung, K. H. Ahn, L. F. Francis, *AIChE J.* **2010**, 56, 2769.
- [74] R. P. Sear, *J. Chem. Phys.* **2018**, 148, 134909.
- [75] R. P. Sear, P. B. Warren, *Phys. Rev. E* **2017**, 96, 62602.
- [76] Y. Tang, G. S. Grest, S. Cheng, *Langmuir* **2018**, 34, 7161.
- [77] M. Haarmann, W. Haselrieder, A. Kwade, *Energy Technol.* **2020**, 8, 1801169.
- [78] W. Haselrieder, S. Ivanov, H. Y. Tran, S. Theil, L. Froböse, B. Westphal, M. Wohlfahrt-Mehrens, A. Kwade, *Progr. Solid State Chem.* **2014**, 42, 157.
- [79] D. Schreiner, J. Lindenblatt, F. J. Günter, G. Reinhart, *Procedia CIRP* **2021**, 104, 91.
- [80] C. Sangrós Giménez, B. Finke, C. Schilde, L. Froböse, A. Kwade, *Powder Technol.* **2019**, 349, 1.
- [81] A. Davoodabadi, J. Li, Y. Liang, R. Wang, H. Zhou, D. L. Wood III, T. J. Singler, C. Jin, *J. Electrochem. Soc.* **2018**, 165, A2493.
- [82] National Center for Biotechnology Information, <https://pubchem.ncbi.nlm.nih.gov/compound/1-Methyl-2-pyrrolidinone> (accessed: August 2023).